Simulating Dispersive Transport in Porous Media and the Influence of Segmentation in Carbonates

F. Gray[1], J. Cen[1], S. M. Shah[1], J.P. Crawshaw[1*] and E.S. Boek[1,2],

[1] *Qatar Carbonates and Carbon Storage Research Centre (QCCSRC), Department of Chemical Engineering, South Kensington Campus, Imperial College London, London SW7 2AZ, United Kingdom.*

[2]*Department of Chemistry, University of Cambridge, Lensfield Road, Cambridge CB2 1EW, UK* *e-mail: esb30@cam.ac.uk*

*j.crawshaw@imperial.ac.uk

Abstract

We introduce a new hybrid simulation model to calculate the hydrodynamic dispersion in pore scale images of real porous media. For this purpose a stochastic particle model for simulating the advection and diffusion of a solute is coupled to a Lattice-Boltzmann algorithm to calculate the flow field in complex geometries. The particle method incorporates second order spatial and temporal resolution to resolve finer features of the domain. We demonstrate how dispersion coefficients can be accurately obtained in capillaries, where corresponding analytical solutions are available, even when these are resolved to just a few lattice units. Then we compute molecular displacement distributions for pore-spaces of varying complexity: a pack of beads; a Bentheimer sandstone; and a Portland carbonate. Our calculated propagator distributions are compared directly with recent experimental PFG-NMR propagator distributions (Scheven *et al*. (2005) and Mitchell *et al*., (2008)), the latter excluding spin relaxation mechanisms. We observe that the calculated transport propagators can be quantitatively compared with the experimental distribution, provided that spin relaxations in the experiment are excluded, and good agreement is found for both the sandstone and the carbonate. However, due to the absence of explicit micro-porosity from the carbonate pore space image used for flow field simulations we note that there are fundamental differences in the physical origins of the stagnant zones for micro-porous rocks between simulation and experiment. We

31 demonstrate how subjectivity in the segmentation process leads to different amounts of

32 stagnancy computed in the same original sample. Finally, we show how the calculations are

33 affected by the presence of isolated pores which arise from the segmentation process.

34 Introduction

35 The hydrodynamic dispersion of solute particles in porous media is of great importance in

36 many scientific and engineering applications (Adler 1992), including ground water pollution,

37 CO_2 sequestration and hydrocarbon recovery. The upscaling of dispersion phenomena from

38 the pore to core scale is complex and a rigorous theoretical description remains an

39 outstanding scientific challenge (Bijeljic and Blunt 2006). Various numerical methods have

40 been proposed to investigate dispersion at the pore scale. Historically, network modelling

41 has been widely used (Bruderer and Bernabé 2001, Bijeljic, Muggeridge *et al.* 2004, Bijeljic

42 and Blunt 2006, Acharya, Van der Zee *et al.* 2007). However, for heterogeneous porous

43 media, such as carbonate rocks, it is very difficult to extract reliable and unique pore

44 networks (Knackstedt, Arns *et al.* 2006). For this reason, direct calculation on three-

45 dimensional pore space images obtained from e.g. micro-CT scanning or Confocal Laser

46 Scanning Microscopy (CLSM) (Shah, Crawshaw et al. 2013) has been proposed to avoid the

47 problems associated with network extraction (Ramstad, Idowu *et al.* 2012). Coelho *et al.*

48 (Coelho, Thovert *et al.* 1997) used a finite difference method to solve for the flow and

49 dispersion in unconsolidated bead packs and sandstones. (Maier, Kroll *et al.* 1998) used a

50 hybrid method, consisting of lattice-Boltzmann (LB) simulations to calculate the flow field

51 combined with a random-walk particle-tracking method to simulate dispersion in a sphere

52 pack. They found good agreement with nuclear magnetic resonance (NMR) experiments for

53 both transient and asymptotic dispersion. Recently, Scheven *et al.* (Scheven, Verganelakis *et*

54 *al.* 2005, Scheven, Harris *et al.* 2007) reported molecular displacement (or propagator)

55 distributions for different rock samples obtained from Pulsed Field Gradient—Nuclear

56 Magnetic Resonance (PFG-NMR) experiments. They observed that the character of the

57 propagator distributions strongly depends on the heterogeneity of the porous medium.

58 Bijeljic *et al.* (Bijeljic, Raeini *et al.* 2013), using a Stokes solver for the flow field and a

59 streamline-based algorithm for solute dispersion, observed agreement with the

60 experimental NMR propagator results (Scheven, Verganelakis *et al.* 2005). Yang *et al.* (Yang

61 and Boek 2013) developed a new LB algorithm to calculate both the flow field and solute

62   dispersion in pore space images of different heterogeneity. They quantified the degree of

63   heterogeneity and calculated the fraction of solute particles trapped by integrating over the

64   stagnant peak (Yang and Boek 2013). However, it appeared to be difficult to study the

65   diffusive coupling for long time scales in a quantitative fashion. For this reason, we propose

66   here a new hybrid algorithm, using LB simulations to solve the flow field coupled with a

67   streamline-based algorithm for solute dispersion. In addition, we propose a second order

68   predictor-corrector scheme for particle advection, which is more accurately able to compute

69   the dispersion of solute in finer features of the pore-space. We observe good agreement

70   with the experimental propagator distributions (Scheven, Verganelakis et al. 2005, Mitchell,

71   Graf von der Schulenburg et al. 2008) for the simpler pore-spaces. However, the

72   aforementioned simulation studies have not considered the importance and influence of

73   the segmentation procedure on the results for micro-porous carbonate samples. We have

74   considered this systematically in the present study.

Method

76   The simulation is performed on a 3-dimensional Cartesian lattice with nodes marked as

77   either fluid or solid describing the geometry. Fluid nodes are associated with a flow vector

78   which is the solution to the incompressible Stokes flow at the centre of the grid element.

79   This flow-field is computed using the single-phase multiple-relaxation-time (MRT) lattice

80   Boltzmann model (d'Humières 2002).

81   The stochastic tracer method consists of transporting particles through the domain in two

82   steps. First, a forward integration along the flow vectors describes the advection part,

83   followed by a random-walk step to simulate diffusion by Brownian motion. To derive the

84   second order advection scheme, we interpolate a second order velocity field around each

85   node's flow vector V_0 using the 6 neighbouring vectors $V_{\pm x,y,z}$ (figure 1). Generally, these

86   polynomials are written as

$$v^i(x,y,z) = V_0^i(a_x^i x^2 + b_x^i x + c_x^i)(a_y^i y^2 + b_y^i y + c_y^i)(a_z^i z^2 + b_z^i z + c_z^i) \qquad (1)$$

87   where $i = x, y, z$ is the component of the flow vector. The position x, y, z is relative to the

88   centre of the node and the grid spacing is such that the distance between the centres of

89   each neighbour is unity. The coefficients a, b and c are to be determined in terms of the
90   neighbouring vectors.

91   We may then impose boundary conditions to calculate the 27 advection coefficients for
92   each node. Two of these conditions are

$$v^i(0,0,0) = V_0^i \tag{2}$$

$$v^i(\pm 1, y, z) = V_{\pm x}^i \tag{3}$$

93   These conditions imply that all the c coefficients are equal to 1, and thus we only need store
94   18 coefficients for each fluid node.

95   Expressions for the a and b coefficients for a case without adjoining solid nodes can then be
96   obtained for each component i in terms of the neighbouring vectors. For the x coefficients

$$a_x^i = \frac{V_x^i + V_{-x}^i}{2V_0} - 1 \tag{4}$$

$$b_x^i = \frac{V_x^i - V_{-x}^i}{2V_0} \tag{5}$$

97   When a neighbouring node is solid, we impose a 0 velocity vector at the boundary, in line
98   with the half-way bounce-back lattice Boltzmann scheme. For a solid at the $+x$ node, the
99   condition is

$$v^i \left(\frac{1}{2}, y, z \right) = 0 \tag{6}$$

100   Then we obtain expressions for the coefficients with different combinations of adjoining
101   solids. For the x coefficients, with a single solid node at $\pm x$

$$a_x^i = \frac{2}{3} \frac{V_{\pm x}^i}{V_0} - 2 \tag{7}$$

$$b_x^i = \pm \frac{1}{3} \frac{V_{\pm x}^i}{V_0} \pm 1 \tag{8}$$

102   For solids at both $+x$ and $-x$

$$a_x^i = 4 \; ; \quad b_x^i = 0 \tag{9}$$

103   These expressions are directly extended to the y and z coefficients.

104   In lowly resolved features of a geometry represented with just a few fluid nodes, calculating
105   the average velocity by naively averaging the flow vectors can introduce systematic error. It
106   should be clarified that the flow vectors from the lattice-Boltzmann algorithm represent the
107   solution to the Navier-Stokes equation at the centre of the fluid node rather than the
108   average flow velocity through the node. Therefore, we can extract a better estimate of the
109   average flow velocity by integrating the 2nd order velocity field over the node volume.

$$v_{av}^i = \iiint v^i(x,y,z)d\boldsymbol{r} \quad = V_0^i\left(1+\frac{1}{12}a_x^i\right)\left(1+\frac{1}{12}a_y^i\right)\left(1+\frac{1}{12}a_z^i\right) \tag{10}$$

110   To transport a particle along the flow-field, we carry out a standard second order accurate
111   predictor-corrector time-step in a similar way to other stochastic approaches (Szymczak and
112   Ladd 2003)

$$\boldsymbol{x}_p(t+dt) = \boldsymbol{x}(t) + \boldsymbol{v}\big(\boldsymbol{x}(t)\big)dt \tag{11}$$

$$\boldsymbol{x}(t+dt) = \boldsymbol{x}(t) + \frac{1}{2}\big[\boldsymbol{v}\big(\boldsymbol{x}(t)\big) + \boldsymbol{v}(\boldsymbol{x}_p)\big]dt \tag{12}$$

113   where $\boldsymbol{x}$ is the position of the particle at time t, $\boldsymbol{x}_p$ is the 'predicted' position of the particle
114   at time $t+dt$ with time-step dt and $\boldsymbol{v}$ is the flow vector calculated from the polynomial
115   function of position in equation (1).

116   Diffusion is simulated by translating the particle over a random-walk vector. The expected
117   distance a diffusing particle will have travelled in 3D random walk given a diffusion
118   coefficient D_m and time-step dt is $L = \sqrt{6D_m dt}$. We generate a spherically isotropic unit
119   vector by taking 2 uniform random variates r_1 and r_2 on [0,1] and apply the following
120   transformation to obtain polar coordinates

$$\varphi = 2\pi r_1 \tag{13}$$

$$\theta = \cos^{-1}(1 - 2r_2) \tag{14}$$

121   These transformations are derived in appendix 1. Finally, we apply the standard
122   transformation to Cartesian coordinates to obtain a random-walk diffusion vector
123   (Mostaghimi, Bijeljic et al. 2012)

$$\begin{bmatrix} dx \\ dy \\ dz \end{bmatrix} = L \begin{bmatrix} sin\theta cos\varphi \\ sin\theta sin\varphi \\ cos\theta \end{bmatrix} \tag{15}$$

124

125

Validation

127   We compute the longitudinal dispersion coefficient of a solute undergoing advection and

128   diffusion in lowly resolved capillaries of three different cross-sections: parallel plates with

129   infinite width, a square channel and a circular capillary. Each has different merits as a test

130   case. The parallel-plates geometry is represented exactly by the Cartesian grid and the

131   Poiseuille flow field is precisely represented to second order. For the square channel, the

132   geometry is again exactly represented although the analytical flow distribution is no longer a

133   finite-order polynomial but given by a convergent series. Finally, the circular capillary is not

134   smoothly represented on the Cartesian lattice (figure 2).

135   The longitudinal dispersion coefficient D, often called dispersivity, is defined as half the

136   time-rate of change in the variance, σ^2, of a solute distribution: $D = \frac{1}{2}\frac{d}{dt}\sigma^2$. It can be shown

137   that for any channel geometry the asymptotic (long time) dispersivity is given by (Chatwin

138   and Sullivan 1982, Dutta and Leighton 2001):

$$\frac{D_m(D - D_m)}{v_{av}^2} = ka^2 \tag{16}$$

139   where v_{av} is the average flow velocity, D_m the molecular diffusivity and a is the radius or

140   half the height of the capillary. The constant k is a dimensionless parameter, which is solely

141   dependent on the cross-sectional geometry of the capillary. For a circular capillary $k = \frac{1}{48}$

142   (Aris 1956, Deen 1998), for parallel-plates with infinite width $k = \frac{2}{105}$ (Deen 1998, Dutta and

143   Leighton 2001), and for a square capillary $k \approx \frac{173}{5250}$ (Doshi *et al.* 1978, Chatwin and Sullivan

144   1982, Dutta and Leighton 2001). The exact value of k for the square capillary can be

145   computed using the equations in the paper by Doshi et al. 1978 or Chatwin & Sullivan 1982.

146   We generate geometries of heights/diameters varying from 1 to 25 lattice units (l.u.) for the

147   three cases of parallel plates ($2a$ is the plate separation), square cross-section capillary ($2a$

148   is the height and width), and circular cross-section capillary ($2a$ is the diameter). We

149   compute the flow-field inside each geometry with lattice Boltzmann simulation and using a

150   uniform body-force. The dispersion coefficient is computed by initialising 10^6 point particles

151   at the flow distance coordinate $x = 0$ uniformly over the cross-section and running the

152   simulation until the dispersion coefficient reaches an asymptotic value. The time-step is

153   chosen such that a particle's maximum displacement is 10% the characteristic length of the

154   medium, i.e. $2a$ in our simulations which corresponds to 0.5 lattice units.

155   Figures 3 and 4 show the simulation results plotted against the analytical expressions and

156   the error from the analytical values respectively for each cross-section and resolution. The

157   error values themselves will have a contribution from the statistical fluctuations of the

158   particle distribution during sampling the asymptotic dispersion coefficient of the order 1%.

159   For the case of parallel plates, we find no systematic deviation from the analytical result, as

160   expected. For the square capillary resolved to a 1 and 2 l.u. dimension, the error stems from

161   fitting a single second order curve to the true infinite order flow-field function. This error

162   decays quickly as the resolution increases and is negligible for resolutions above 5 l.u. For

163   the circular case, the diameter is not well defined in the small blocky geometries and so we

164   have extracted an effective value from the true cross-sectional area A such that $2a =$

165    $\sqrt{4A/\pi}$. The deviation from the analytical result is most pronounced in this case, yet

166   generally below 10% above a 5 l.u. diameter and gradually decreasing over the larger

167   dimensions.

168   Propagator Distributions

169   We now use the model to compute molecular displacement distributions inside images of

170   real pore-spaces. Three cases are examined, of varying complexity: a pack of beads

171   exhibiting high regularity and connectivity; a Bentheimer sandstone with a non-

172   homogeneous but well-connected structure; and a Portland carbonate with a

173   heterogeneous pore-space. Samples were obtained from micro-CT imaging, followed by

174   segmentation on a Cartesian lattice of solid and pore voxels (Blunt, Bijeljic *et al.* 2012). In

175   highly micro-porous carbonate rocks, this segmentation procedure can be subjective and its

176   effects are considered in this work.

177   The three porous media chosen allow us to compare the results of simulation with the

178   experimental NMR data of Scheven *et al.* (Scheven, Verganelakis *et al.* 2005) for the three

179   samples, and the spin loss-corrected data of Mitchell *et al. (Mitchell, Graf von der*

180   *Schulenburg et al. 2008)* for the Bentheimer and Portland samples. Representative samples

181   are chosen and given in table 1 (Shah 2014)

Sample	Dimension (mm)	Size (Voxels)	Resolution (μm)	Porosity
Beadpack	0.625	250^3	2.50	37.9%
Bentheimer	1.810	400^3	4.52	20.9%
Portland	1.810	400^3	4.52	13.7%

182   Table 1 – Samples used in the simulation

183   The beadpack consists of spheres of 86 ± 10μm, which we have found to give the best

184   quantitative fit to the NMR data, in which beads of 100 ± 20μm are reportedly used. We

185   have applied the mirroring concept to these samples to guarantee flow and transport

186   continuity over the boundaries (Yang and Boek 2013). In this approach, the samples are

187   reflected about the $x = 0$ axis, where x is the flow direction. Thus the computational

188   domain size is now doubled, for example, 500x250x250 lattice units for the beadpack.

189   The calculations are performed by initialising a set of tracer particles uniformly throughout

190   each medium and computing the displacement of each particle from its initial position. A

191   displacement density function can then be obtained at different sample times, or

192   equivalently, mean Darcy displacements $d = v\Delta t$ where v is the mean Darcy velocity in the

193   pore-space and Δt is the sample time. The two experimental papers obtain data in different

194   ways: Scheven *et al.* employ a constant flow rate, sampling the displacement distribution at

195   different times whereas Mitchell *et al.* sample the distribution at a fixed time of $\Delta t = 1s$ for

196   a set of different flow rates. The diffusion coefficient of water at ambient temperature is

197   used: $D_m = 2.0x10^{-9}m^2s^{-1}$, and the timescale is derived by matching the experimental

198   mean Darcy flow velocities or flow rates.

199   The distributions are shown for each medium at 3 different sample distances in figures 5, 6,

200   and 7 respectively, overlaid with the corresponding NMR data from Scheven *et al.* (Scheven,

201   Verganelakis *et al.* 2005) for the beadpack and Mitchell *et al.* (Mitchell, Graf von der

202   Schulenburg et al. 2008) for the sandstone and carbonate. Scheven *et al.* also computed

203   propagators for Bentheimer and Portland samples which include the influence of spin-

204   relaxation. This is demonstrated by comparing the time-dependent mean particle

205   displacements in the experiment to calculations performed by imposing the same mean

206   Darcy flow velocity in the samples. Figure 8 shows the mean displacement of the solute

207   particles, $\langle x \rangle$ relative to the mean Darcy displacement for each medium, and may be

208   compared with Scheven's experimental data. Our calculations imply that the mean particle

209   displacement is very close to the Darcy displacement: $\frac{\langle x \rangle}{d} \approx 1$ for all cases whereas the

210   experimental ratios converge to 1.03 (beadpack), 1.2 (Bentheimer) and 1.3 (Portland). In

211   later publications, the authors of the experimental NMR work considered this to be due to

212   loss of spins, particularly close to solid grain boundaries and is thus most pronounced in the

213   micro-porous carbonate (Scheven, Seland *et al.* 2004, Mitchell, Graf von der Schulenburg *et*

214   *al.* 2008, Hussain, Mitchell *et al.* 2013). To solve this problem, Mitchell *et al.* (2008) have

215   obtained flow propagators excluding the influence of NMR relaxation times T1 and T2.

216   These spin relaxation mechanisms usually give a loss of signal that depends on the

217   displacement of the flowing spins. The exclusion of T1 and T2 allowed acquisition of

218   quantitative propagator data (Mitchell *et al.* (2008)). For this reason, we directly compare in

219   figure 6 our calculated propagators for the Bentheimer sandstone and micro-porous

220   Portland carbonate, with the recent experimental propagator data obtained by Mitchell *et*

221   *al.* (2008). We note that to obtain different displacements in this set of NMR experiments

222   the flow rate was changed and the time interval for acquisition kept constant. This resulted

223   in a range of Peclet numbers, in contrast to the simulations of the beadpack in which the

224   flow rate and therefore the Peclet number was kept constant.

225   With the adjusted mean, the beadpack distributions agree well with the experimental data

226   which converges to a Gaussian distribution. Two statistical measures are useful for

227   quantifying the convergence behaviour: the Skewness and Kurtosis Excess, defined as

$$\gamma = \frac{\mu_3}{\mu_2^{3/2}} \quad and \quad \kappa = \frac{\mu_4}{\mu_2^2} - 3 \qquad (17)$$

228   where μ_i is the ith central moment of the distribution, such that μ_2 is recognised as the

229   variance. The skewness measures the symmetry of a distribution about the mean and the

230   kurtosis excess is a measure of peakedness: 0 for a Gaussian distribution; <0 for a more

231   sharply peaked distribution; and >0 for a flatter distribution. These are shown in figure 9 for

232   the beadpack which are seen to be converging towards 0, implying that the beadpack

233   distribution tends towards a Gaussian in the long-time limit.

234   The time-dependent skewness of the Bentheimer and Portland distributions are also given

235   in figure 10 using the experimental parameters of Scheven et al. Since we can identify two

236   peaks in the propagator distributions (figures 6 and 7) of these samples: a stagnant

237   component about zero displacement and a moving peak around the mean displacement,

238   the kurtosis excess is not meaningful in these cases. The Bentheimer skewness tends

239   towards 0 on a longer timescale than the beadpack and in accordance with the observation

240   that the stagnant peak in the propagator distribution decreases with time as solute in less-

241   well-connected areas of the pore structure diffuse into flowing regions. The carbonate

242   distributions however are not seen to become symmetric over the time-scale examined.

243   This observation is further quantified by measuring the fraction of solute which is contained

244   in the stagnant peak of the propagator distributions over time. We adopted the following

245   measure of this fraction, $S(t)$

$$S(t) = 2 \int_{-\infty}^{0} P(x', t) \, dx' \qquad (18)$$

246   where x' is the scaled unit x/d and we are assuming that the stagnant peak is symmetric

247   about zero displacement. The stagnant fractions against time for the three samples are

248   given in figure 11 using the experimental parameters of Scheven et al. The beadpack

249   stagnant fraction disappears the most quickly, but is not immediately 0. This can be seen in

250   the early propagator distribution figure 5a as the slightly pronounced bump at the zero

251   displacement and might reasonably be explained as the small amount of solute in the

252   immediate vicinity behind beads having to diffuse a short way into a flowing streamline. The

253   stagnant component in the sandstone appears to decay to almost zero on the simulation

254   time-scale, but takes considerably longer than the beadpack, reflecting the increased

255   complexity of the sandstone structure. Nonetheless, this implies that the pore structure is

256   completely connected. The same conclusion cannot be drawn for the carbonate, whose

257   stagnant fraction asymptotically persists as around 20% of the normalised distribution. This

258   suggests that a similar fraction of the pore-space has no connection to a flowing path

259   through the domain. Such an effect may be an artefact of the image segmentation process,

260   rather than a physical one. We also note that the stagnant fractions for the beadpack and

261   sandstone samples match the NMR data of Scheven *et al.* very closely, suggesting that

262   spurious spin relaxation mechanisms are at least uniform over the displacement

263   distributions. The stagnant peak is greatly over-predicted in the carbonate sample which is

264   consistent with experimental spin losses being most pronounced in the low-flow micro-

265   porous regions.

266   Figure 12 gives the stagnant fractions computed for the Bentheimer and Portland samples

267   for the Peclet numbers (flow rates) alongside the loss-corrected NMR data of Mitchell *et al.*

268   (2008). The trapped fraction in the Bentheimer is again seen to reach near-zero as the flow

269   rate (flow distance at $t = 1s$) increases with Peclet number. The carbonate once again

270   apparently reaches an asymptotic trapped fraction of $20\% - 25\%$. Agreement with the

271   experimental NMR data is relatively good but differences in the Bentheimer propagator

272   distributions (figure 6a,b and c) suggests some uncertainty in matching the flow rates or

273   diffusion coefficients with experiment. Nonetheless, the stagnant peak of the carbonate is

274   much more closely matched as would be expected from excluding spin-loss effects

275   concentrated in the micro-porous zones.

276   Despite the quantitative agreement, there are important differences between the

277   simulations and experiment for the Portland carbonate which need to be pointed out.

278   Chiefly, we note that simulation is performed on a segmented version of the pore-space. As

279   such, any transport through micro-porous zones in the experiment is not incorporated into

280   the calculation, but binarized into either fully permeable porous zones, or impermeable

281   solid phase. This process in inherently subjective and we now demonstrate this

282   systematically, returning to the time-dependant calculation of stagnant peaks which helps

283   to elucidate the connectivity of the pore-space.

284   The segmentation process takes a continuum-valued (grey-scale) image from a micro-CT

285   scan and converts this to a discrete set of phases. In general the principle for all

286 segmentation methods is based on separating the phases by detecting similarities and
287 discontinuities in intensity grey value and partitioning the phases accordingly with the help
288 of different edge detection algorithms and labelling similar regions of each phase. In this
289 study, a non-local means filter followed by a seeded watershed algorithm was used to
290 segment the images into 2 phases: pore and grain (Jones, Arns et al. 2009, Andrew, Bijeljic
291 et al. 2013, Shah, Crawshaw et al. 2013). A seeded watershed algorithm relies not only on
292 the intensity of an image but also on the gradient magnitude of an image with the seed
293 generated by the use of 2D histograms. The 2D Histogram Segmentation module within the
294 Avizo Fire 8.0 program has two main processes: (1) initialization of voxels into two or more
295 phases using the concept of the region growing method based on 3D voxel intensity and
296 gradient magnitude and (2) expansion of initially assigned voxels in step 1 so that all the
297 voxels are labelled using the watershed transform. For highly micro-porous samples, the
298 histogram data in step 1 is not sharply defined, so that the researcher's choice may play a
299 role in the result.

300 To highlight the subjectivity of this process further, we took the same initial grey-scale
301 image of Portland carbonate and performed four new segmentations leading to a range of
302 porosities 9.0%, 12.9%, 15.0% and 17.9%. Figure 13 shows a slice of the original image along
303 with the equivalent segmented result. Also highlighted is an example of a clearly micro-
304 porous grey-scale zone segmented into pore in the 12.9% porosity sample, but as a solid
305 zone in the 9.0% sample.

306 The flow rate used was that of Scheven *et al*. (ref.). The stagnant fraction was computed
307 again by equation 18 and the result shown against time in figure 14. The discrepancy
308 between the different samples is immediately obvious, a factor of more than 2 difference
309 between the lowest and highest porosities. The lowest porosity sample had the highest
310 fraction of stagnant solute over the simulation, with a gradually decreasing trapped fraction
311 with increasing porosity. The physical interpretation is less clear. We might expect that in
312 the lowest porosity sample, only fully porous areas of the original image have been
313 segmented into pore-space and a few of the most porous micro-pore zones. As the porosity
314 of the segmented images increases, more of the micro-porous (grey-scale) areas are
315 included. These pores of micro-porous origin would be expected to have the highest
316 likelihood of being isolated from flowing zones, and thus comprise permanently trapped

317 solute. This then suggests that stagnant zone of the 9.0% porous sample should decay most

318 fully in the long-time limit and the higher porosity images should reach asymptotic values

319 increasing with porosity.

320 Whether such behaviour is observed in reality is beyond the time-scale of our simulations.

321 However it is possible to illuminate this issue further. As a final analysis, we applied a

322 filtering algorithm to each image which removed isolated pores i.e. any pore not percolating

323 to a flowing face through at least one of its 6 Cartesian neighbours. A comparison of

324 stagnant fractions between filtered and unfiltered images is given in figure 15. The order of

325 the curves is maintained: the 9.0% sample most stagnant and the 17.9% sample the least so.

326 However, where the curves for the 3 highest porosity samples are consistently lower in the

327 filtered image (consistent with discounting the permanently trapped solute), the 9.0%

328 porous sample maintains roughly the same profile in both filtered and unfiltered

329 simulations. This confirms that most or all of the stagnant solute in this image is not

330 permanently trapped, but should diffuse out of slow regions after a longer time. On the

331 other hand, the higher porosity segmentations do contain isolated stagnant zones so that

332 the curves in the unfiltered cases should eventually reach an asymptotic, non-zero value.

333 Finally, the slower decay of the 9.0% porous sample indicates that the flowing pore-space is

334 more constricted, becoming less so with increasing porosity.

Conclusion

336 We detailed a stochastic transport simulation method able to resolve the velocity field

337 smoothly in fine areas of a simulation domain. This was compared with the analytical

338 dispersion results in capillaries and shown to be accurate even with very lowly resolved

339 channels.

340 Using this method, it was possible to match transport propagators to corresponding NMR

341 experimental data quantitatively for a beadpack and sandstone. For the micro-porous

342 Portland carbonate sample, we compared our calculated propagator distributions directly

343 with recent experimental propagator distributions (Mitchell *et al.*, (2008)). These

344 measurements excluded spin relaxation mechanisms associated with NMR relaxation times

345 $T1$ and $T2$, thus allowing acquisition of quantitative propagator data (Mitchell *et al.* (2008)).

346 Indeed, this comparison shows that the calculated transport propagators can be semi-

347   quantitatively compared with the experimental distribution, provided that spin relaxations

348   in the experiment are excluded, but note that the experiment and simulations are not

349   entirely physically consistent because stagnant zones arising from micro-pores are not

350   included in the simulation, but instead stem from badly-connected or isolated macro-pores

351   which can depend on the segmentation procedure.

352   For such geometries whose transport behaviour is strongly influenced by micro-porous

353   zones, models which incorporate continuum porosity and permeability grid cells are more

354   appropriate. If effective dispersion coefficients can be assigned to micro-porous areas,

355   combined with a probabilistic entry/exit scheme for particles crossing from porous to micro-

356   porous zones, the transport behaviours can be more accurately predicted, thus avoiding

357   subjective segmentation procedures.

362

363

364

365

366

367

368

369

370   Figures
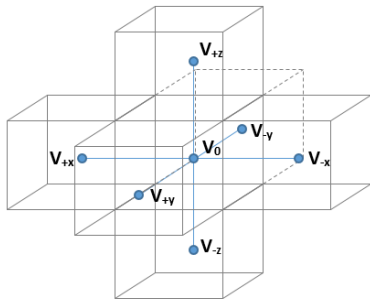
371

372   Fig 1. Centre node velocity vector $\mathbf{V}_0$ and its 6 nearest neighbours
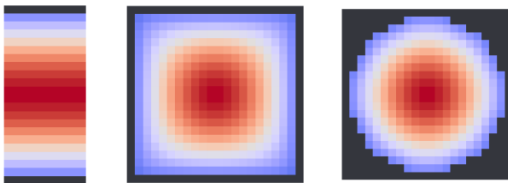
373

374   Fig 2. Capillaries of differing cross-section: parallel plates, square channel and circular cross-section

375   of height (diameter) 20 lattice units. Velocity profiles range from fastest zones in red to slowest in

376   blue.
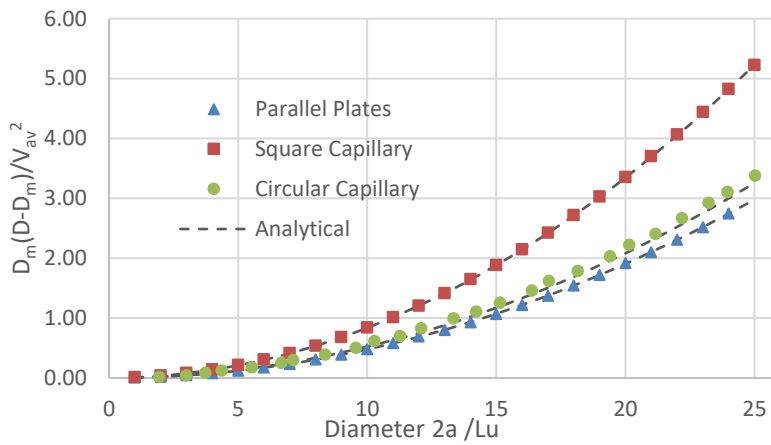
377

378   Fig 3. The value of ka^2 computed for capillaries of the given cross-sections compared to the

379   analytical solution.
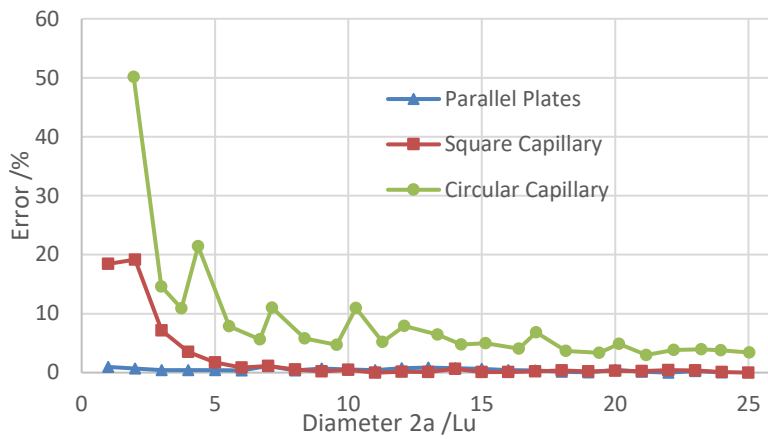
380

381   Fig 4. The percentage error in the calculation relative to the exact expression. These values

382   themselves are subject to an error of ±1% because of the statistical fluctuation of the particle

383   distribution
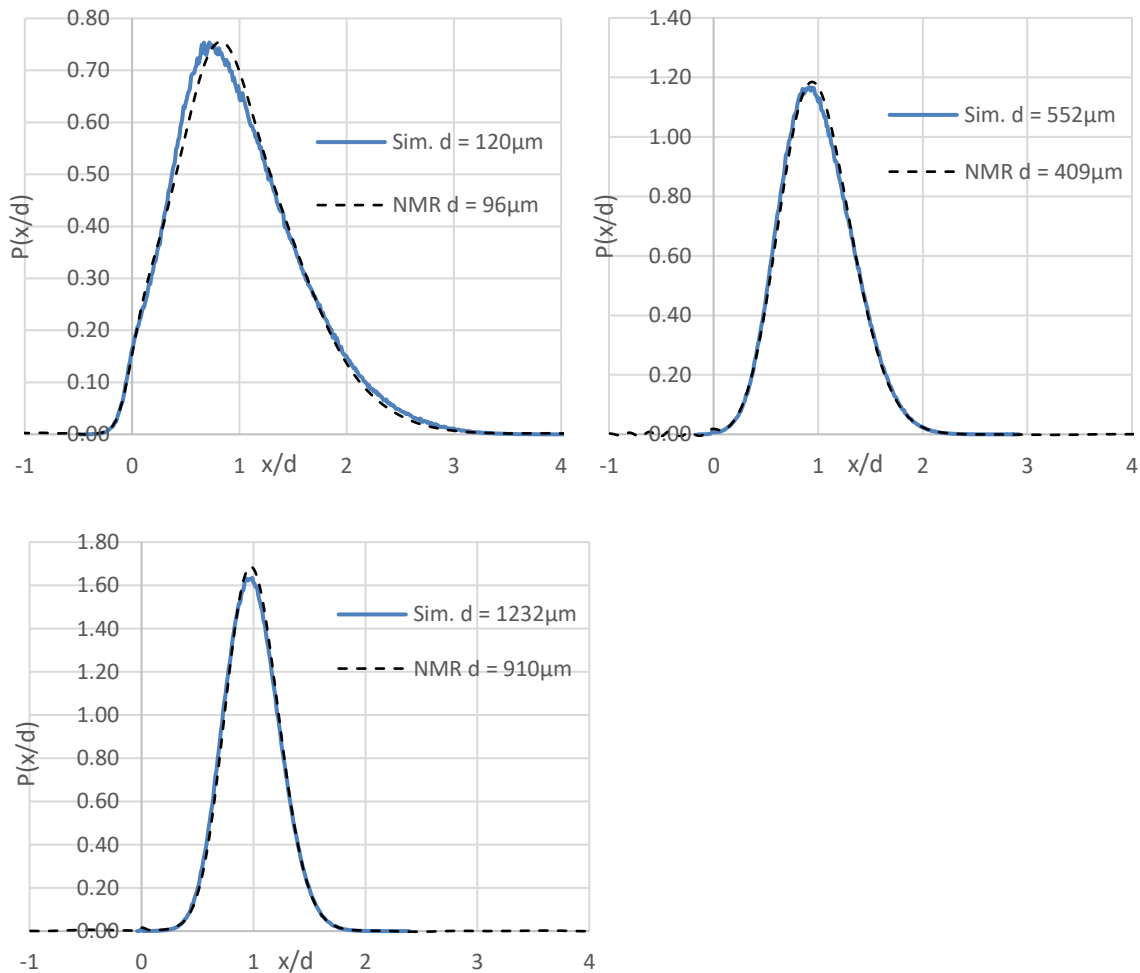
384

385

386   Fig 5a, b, c. Propagator distribution in Beadpack at different sample times compared to the NMR

387   results of *Scheven et al.* (2005) (dashed lines).

388

389

390
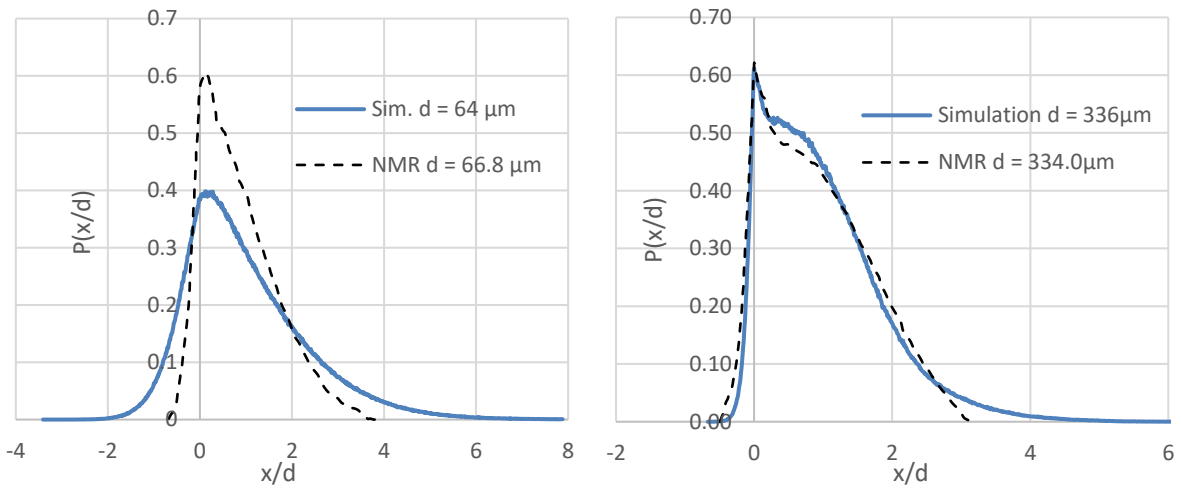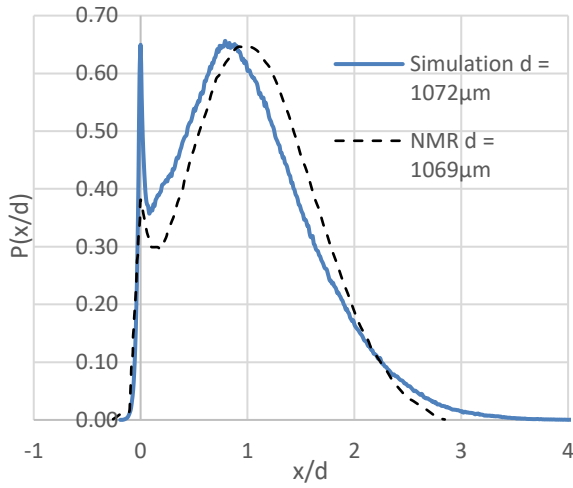
Fig 6a, b, c. Propagator distribution in Bentheimer sandstone at the same sample time (t = 1s) with increasing flow rates and Peclet numbers: a) Pe = 5; b) Pe = 64; c) Pe = 81. Calculated distributions are indicated with a blue line, in comparison with the propagator data obtained by Mitchell *et al.* (2008), indicated by a black dashed line.

395

396

397

398

399
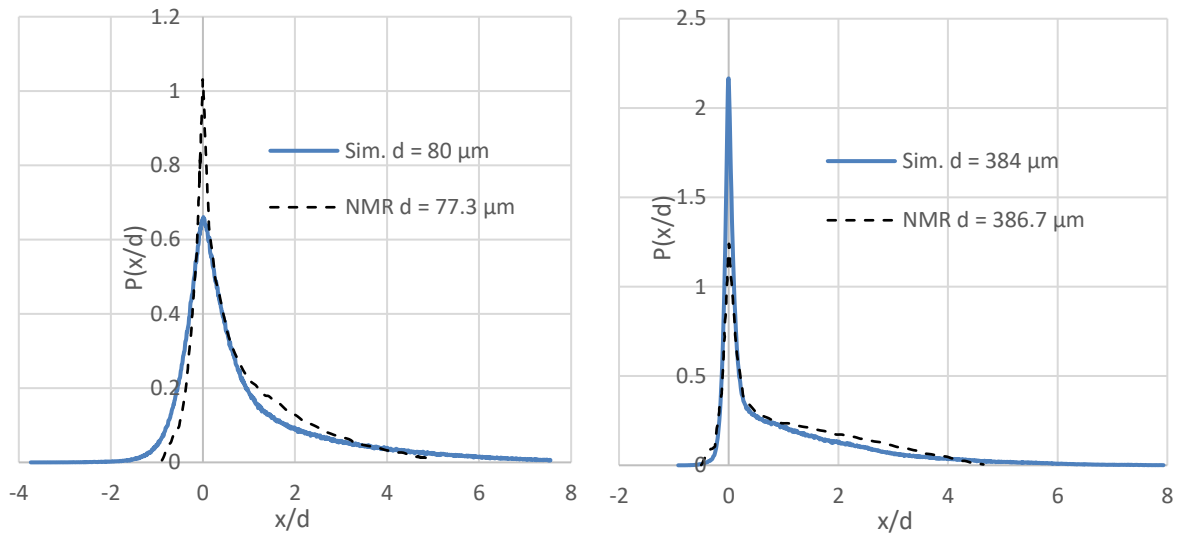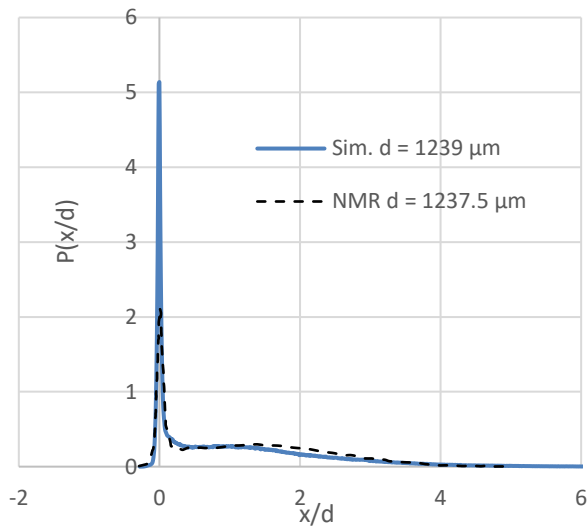
Fig 7a, b, c. Propagator distribution in Portland carbonate at the same sample time (t = 1s) with increasing flow rates and Peclet numbers: a) Pe = 7.2; b) Pe = 36; c) Pe = 116. Calculated distributions are indicated with a blue line, in comparison with the propagator data obtained by Mitchell *et al.* (2008), indicated by a black dashed line. Isolated pores are present in the calculations, which add to the stagnant peak. The segmented image porosity is 13.5%.
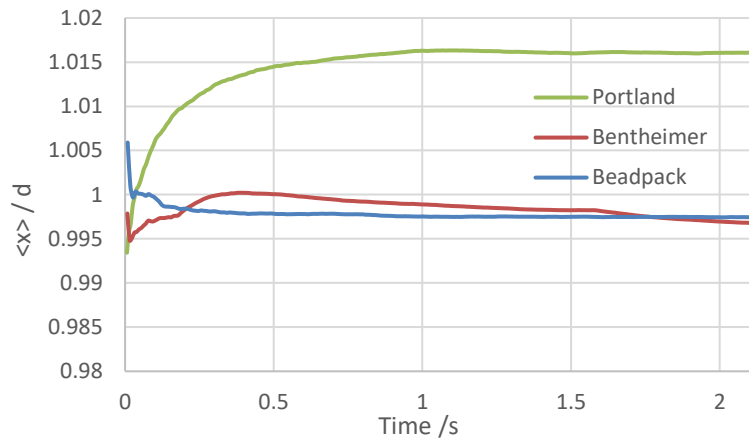
405

406 Fig 8. Computed mean particle displacement relative to mean Darcy displacement. Parameters
407 match the experimental values used by Scheven et $al.$: constant mean Darcy flow rates of 910μms^{-1}
408 (beadpack), 1030μms^{-1} (Bentheimer) and 1260μms^{-1} (Portland) sampled over time.
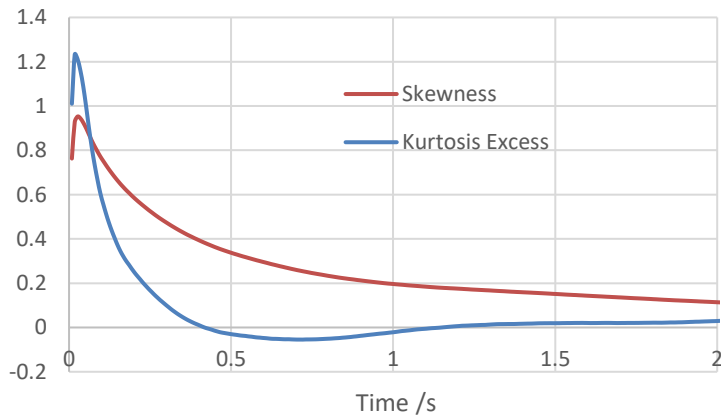
409

410 Fig 9. Kurtosis Excess and Skewness of propagators computed for the beadpack propagator
411 distribution over time with a flow rate of 910μms^{-1}.
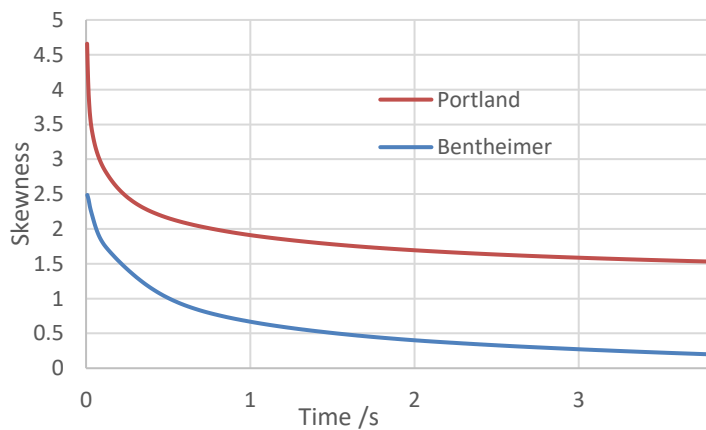
412

413   Fig 10. Skewness computed for propagators of Bentheimer sandstone and Portland carbonate with

414   parameters used by Scheven *et al.*: mean Darcy velocities of 1030µms^{-1} (Bentheimer) and 1260µms^{-1}

415   (Portland) sampled over time.
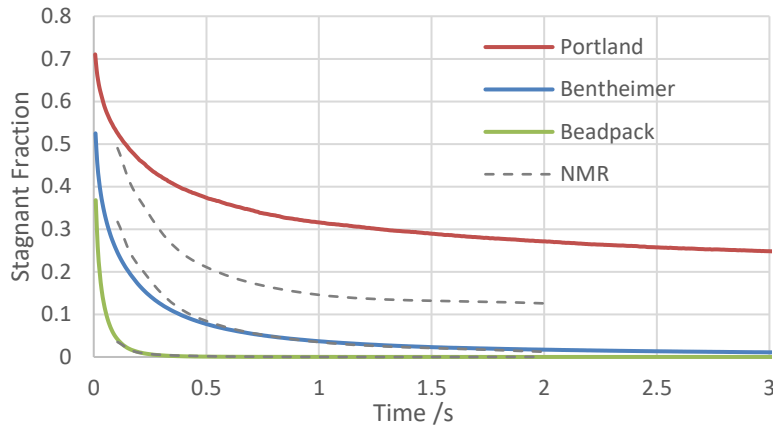
416

417   Fig 11. Fraction of solute stagnant over time computed for the three samples using the experimental

418   parameters and against the NMR data of Scheven *et al*.
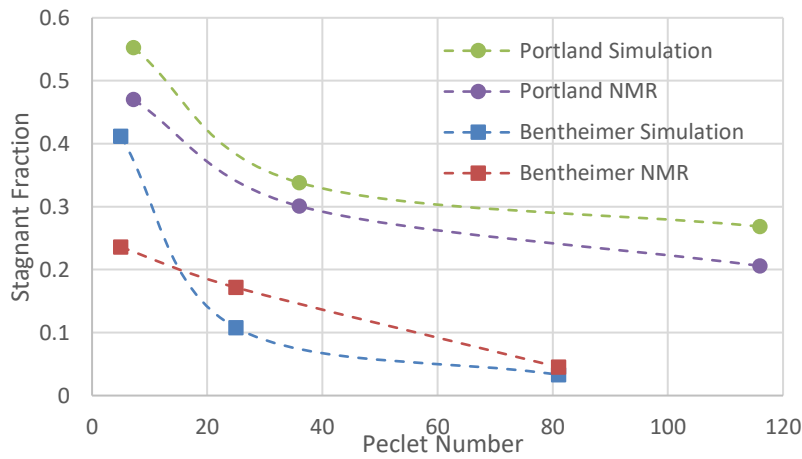

419

420   Fig 12. Fraction of solute stagnant over time computed for the Bentheimer and Portland samples

421   against Peclet number using the parameters and against the NMR data of Mitchell *et al.*

422
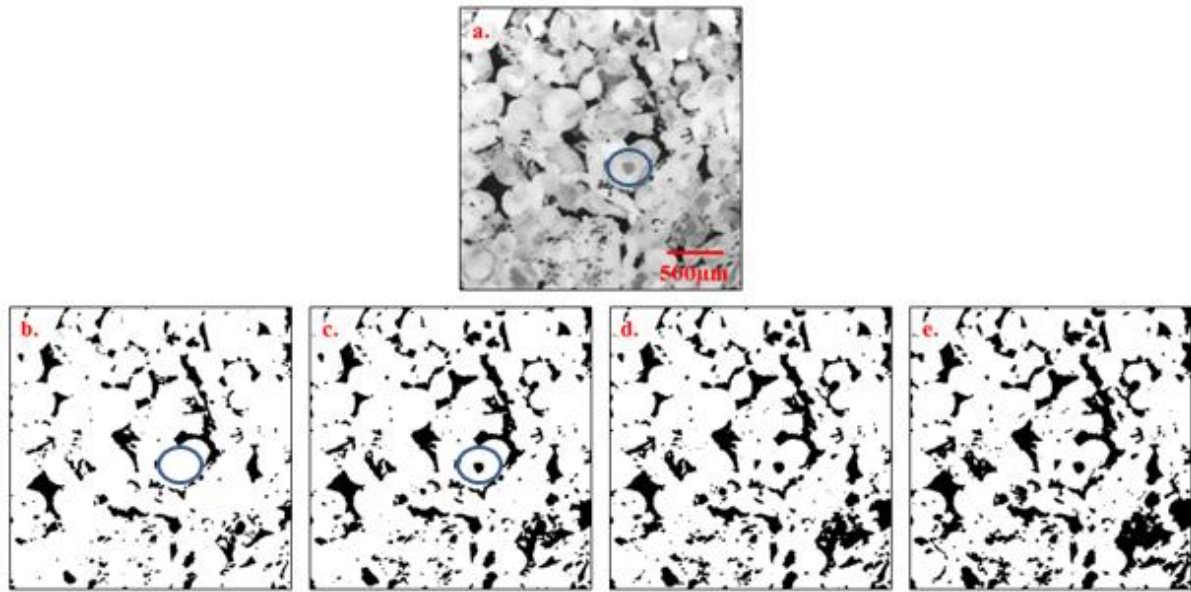
Figure 13. Two-dimensional cross-section of three dimensional micro-CT image of Portland carbonate. (a) Original image. (b) Segmented porosity – 9 %. (c) Segmented porosity – 12 %. (d) Segmented porosity – 15 %. (e) Segmented porosity – 18 %. Circled in a), b), and c) – a microporous region segmented into macro-pore as the segmented porosity is increased from 9% to 12%.

427

428
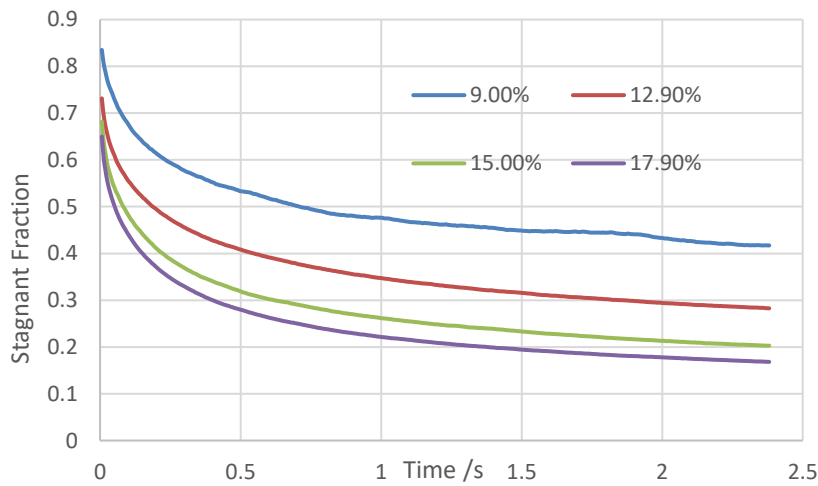
Fig 14. Fraction of solute stagnant over time for different segmentations of Portland carbonate, labelled by their porosity.

431
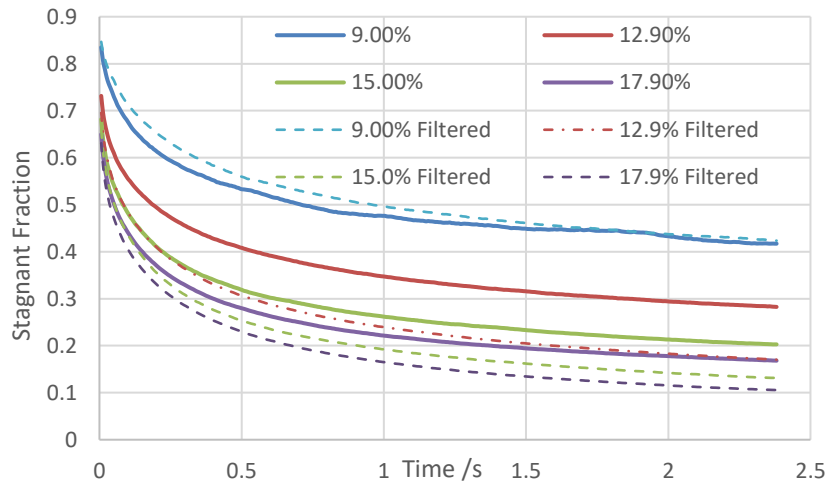
Fig 15. Fraction of solute stagnant for Portland carbonate overlaid with data from filtered images

(isolated pores removed) and labelled by the unfiltered image porosity.

References

Acharya, R., et al. (2007). "Approaches for modeling longitudinal dispersion in pore-networks." Advances in Water Resources **30**(2): 261-272.

Adler, P. M. (1992). Porous media: geometry and transports, Butterworth-Heinemann.

Andrew, M., et al. (2013). "Pore‐scale imaging of geological carbon dioxide storage under in situ conditions." Geophysical Research Letters **40**(15): 3915-3918.

Bijeljic, B. and M. J. Blunt (2006). "Pore-scale modeling and continuous time random walk analysis of dispersion in porous media." Water Resources Research **42**(1): n/a-n/a.

Bijeljic, B., et al. (2004). "Pore‐scale modeling of longitudinal dispersion." Water Resources Research **40**(11).

Bijeljic, B., et al. (2013). "Predictions of non-Fickian solute transport in different classes of porous media using direct simulation on pore-scale images." Physical Review E **87**(1): 013011.

Blunt, M. J., et al. (2012). "Pore-scale imaging and modelling." Advances in Water Resources.

Bruderer, C. and Y. Bernabé (2001). "Network modeling of dispersion: Transition from Taylor dispersion in homogeneous networks to mechanical dispersion in very heterogeneous ones." Water Resources Research **37**(4): 897-908.

Coelho, D., et al. (1997). "Geometrical and transport properties of random packings of spheres and aspherical particles." Physical Review E **55**(2): 1959.

d'Humières, D. (2002). "Multiple–relaxation–time lattice Boltzmann models in three dimensions." Philosophical Transactions of the Royal Society of London. Series A: Mathematical, Physical and Engineering Sciences **360**(1792): 437-451.

Hussain, R., et al. (2013). "Monitoring water transport in sandstone using flow propagators: A quantitative comparison of nuclear magnetic resonance measurement with lattice Boltzmann and pore network simulations." Advances in Water Resources **60**: 64-74.

Jones, A. C., et al. (2009). "The correlation of pore morphology, interconnectivity and physical properties of 3D ceramic scaffolds with bone ingrowth." Biomaterials **30**(7): 1440-1451.

Knackstedt, M., et al. (2006). "3D imaging and flow characterization of the pore space of carbonate core samples."

Maier, R. S., et al. (1998). "Simulation of flow through bead packs using the lattice Boltzmann method." Physics of Fluids (1994-present) **10**(1): 60-74.

Mitchell, J., et al. (2008). "Determining NMR flow propagator moments in porous rocks without the influence of relaxation." Journal of Magnetic Resonance **193**(2): 218-225.

Mostaghimi, P., et al. (2012). "Simulation of flow and dispersion on pore-space images." SPE Journal **17**(4): 1131-1141.

Ramstad, T., et al. (2012). "Relative permeability calculations from two-phase flow simulations directly on digital images of porous rocks." Transport in Porous Media **94**(2): 487-504.

Scheven, U., et al. (2007). "Intrinsic dispersivity of randomly packed monodisperse spheres." Physical review letters **99**(5): 054502.

Scheven, U., et al. (2004). "NMR propagator measurements on flow through a random pack of porous glass beads and how they are affected by dispersion, relaxation, and internal field inhomogeneities." Physical Review E **69**(2): 021201.

Scheven, U., et al. (2005). "Quantitative nuclear magnetic resonance measurements of preasymptotic dispersion in flow through porous media." Physics of Fluids **17**(11): 7107.

Shah, S. M., Yang, J., Gray, F., Crawshaw, J.P. & Boek, E.S. (2014). "Determining Representative Elementary Volume using Pore Scale Imaging and lattice Boltzmann Modelling." Ready to be submitted to Geophysical Research Letters. .Awaiting sponsors decision for patent filing.

501 Shah, S. M. K., et al. (2013). <u>Predicting Porosity and Permeability of Carbonate Rocks From Core-</u>
502 <u>Scale to Pore-Scale Using Medical CT Confocal Laser Scanning Microscopy and Micro CT</u>. SPE Annual
503 Technical Conference and Exhibition, Society of Petroleum Engineers.

504

505 Szymczak, P. and A. Ladd (2003). "Boundary conditions for stochastic solutions of the convection-
506 diffusion equation." <u>Physical Review E</u> **68**(3): 036704.

507

508 Yang, J. and E. S. Boek (2013). Quantitative determination of molecular propagator distributions for
509 solute transport in homogeneous and heterogeneous porous media using lattice Boltzmann
510 simulations. <u>Unpublished</u>.

511

512 Appendix 1

513 We have the area of a small surface element, dS on a sphere in terms of the radial distance r,
514 azimuthal angle θ on the range $[0, \pi]$ and the polar angle φ on the range $[0, 2\pi]$

$$dS = r^2 sin\theta d\theta d\varphi \tag{A1.1}$$

515 A random isotropic point on the spherical surface has the following probability of being in the
516 infinitesimal ranges $[\theta, \theta + d\theta]$ and $[\varphi, \varphi + d\varphi]$

$$P(\theta, \varphi)d\theta d\varphi = \frac{dS}{4\pi r^2} = \frac{1}{4\pi} sin\theta d\theta d\varphi \tag{A1.2}$$

517 We require the probability to be the same everywhere and therefore we will equate the cumulative
518 probability for the respective variables with those of uniform variates. The cumulative probability
519 distribution is thus

$$P_c(\theta, \varphi) = \int_0^\theta d\theta \int_0^\varphi d\varphi \ P(\theta, \varphi) = \frac{1}{4\pi}(1 - cos\theta)\varphi \tag{A1.3}$$

520 The complete cumulative probability distributions for the variables φ and θ are therefore
521 respectively

$$P_c(\pi, \varphi) = \frac{1}{2\pi}\varphi \tag{A1.4}$$

$$P_c(\theta, 2\pi) = \frac{1}{2}(1 - cos\theta) \tag{A1.5}$$

522 For a random variate r_i, uniformly distributed over the interval $[0, 1]$, we have the probability of
523 being in the range $[r_i, r_i + dr_i]$ and the cumulative probability respectively

$$P(r_i)dr_i = dr_i \tag{A1.6}$$

$$P_c(r_i) = r_i \tag{A1.7}$$

524 Finally, taking two uniform random variates r_1 and r_2, we equate these with the cumulative
525 probability distributions for φ and θ respectively to obtain expressions for random spherical
526 coordinates in terms of uniform distributions

$$\varphi = 2\pi r_1 \qquad\qquad \text{A1.8}$$

$$\theta = \cos^{-1}(1 - 2r_2) \qquad\qquad \text{A1.9}$$

527